Fizyka Nyzkykh Temperatur/Low Temperature Physics, 2023, Vol. 49, No. 11, pp. 1423–1434

Structure and cryogenic mechanical properties of severely deformed nonequiatomic alloys of Fe–Mn–Co–Cr system

E. D. Tabachnikova[1], T. V. Hryhorova[1], S. N. Smirnov[1], I. V. Kolodiy[2], Yu. O. Shapovalov[1], A. V. Levenets[2], S. E. Shumilin[1], I. V. Kashuba[1], M. A. Tikhonovsky[2], F. Spieckermann[3], M. J. Zehetbauer[4], E. Schafler[4], Y. Huang[5], and T. G. Langdon[6]

[1]*B. Verkin Institute for Low Temperature Physics and Engineering of the National Academy of Sciences of Ukraine Kharkiv 61103, Ukraine*

[2]*National Science Center Kharkiv Institute of Physics and Technology, Kharkiv 61108, Ukraine*

[3]*Department of Materials Science, Chair of Materials Physics, Montanuniversität Leoben, Leoben 8700, Austria*

[4]*Faculty of Physics, University of Vienna, Wien 1090, Austria*

[5]*Department of Design and Engineering, Faculty of Science and Technology, Bournemouth University Poole, Dorset BH12 5BB, UK*

[6]*Department of Mechanical Engineering, University of Southampton, Southampton SO17 1BJ, UK*

E-mail: tabachnikova@ilt.kharkov.ua

Received June 7, 2023, published online September 26, 2023

The work is devoted to a study of the structure and mechanical properties of two nonequiatomic medium-entropy nanocrystalline alloys, in which in a coarse state additional mechanisms act during plastic deformation — twinning (TWIP) in the $Fe_{40}Mn_{40}Co_{10}Cr_{10}$ alloy and phase transformations (TRIP) in the $Fe_{50}Mn_{30}Co_{10}Cr_{10}$ alloy. The nanocrystalline state in these alloys is achieved by high-pressure torsion (HPT) at 300 K and 77 K after different numbers of revolutions $n = 0.25$ and 5. In the nanostructural state in the TWIP $Fe_{40}Mn_{40}Co_{10}Cr_{10}$ and the TRIP $Fe_{50}Mn_{30}Co_{10}Cr_{10}$ alloys, a basically complete phase transition from the fcc lattice to hcp is observed, the content of which does not depend very strongly on the HPT temperature and deformation. For both alloys in the nanostructured state, there is a significant decrease in differences in the phase composition and microhardness H_v by comparison with the coarse-grained state. A decrease in the HPT temperature and an increase in HPT deformation for all the cases studied lead to an increase in the value of H_v. The $Fe_{40}Mn_{40}Co_{10}Cr_{10}$ TWIP alloy remains ductile under active compression deformation at 300 and 77 K, while there is no macroscopic plasticity in the $Fe_{50}Mn_{30}Co_{10}Cr_{10}$ TRIP alloy under similar conditions. For the $Fe_{40}Mn_{40}Co_{10}Cr_{10}$ TWIP the thermally-activated character of plastic deformation is retained during the transition from the coarse-grained to the nanostructured state.

Keywords: high entropy alloys, microstructure, cryogenic temperatures, mechanical properties.

1. Introduction

In recent decades, the physical and mechanical properties of a new class of materials, multicomponent high-entropy alloys (HEA) [1–10], have been actively studied and these have a number of advantages over traditional alloys. The improvement in the physico-mechanical properties of HEAs is usually associated with the features of their structure due, in particular, to higher values of the entropy of mixing compared to traditional multicomponent alloys [11]. According to classical thermodynamics, the entropy of mixing between soluble components is maximum when these components are in equiatomic concentrations [11]. The value of the entropy of mixing in single-phase equiatomic multicomponent alloys increases with an increase in the number of components included in such a system. The HEA crystal

lattice, which consists of atoms of heterogeneous elements with different electronic structures and different sizes, is significantly distorted compared to the ideal lattice out of homogeneous atoms. This approach is confirmed in the well-studied equiatomic HEA CoCrFeMnNi [5, 12–16], which exhibits enhanced mechanical properties compared to traditional alloys: high strength, high ductility, and high fracture toughness, especially at cryogenic temperatures. The high cryogenic strength (≈ 1280 MPa) and plasticity (≈ 70%) of this HEA are associated with the simultaneous action of two mechanisms, slip and twinning, whose significant contribution is especially pronounced at low temperatures [12]. As shown by the results of the mechanical properties studies of HEAs in recent years [5–10, 17–31], the maximum entropy of mixing is not a necessary factor for achieving high mechanical properties. These studies show that in many nonequiatomic HEAs, as well as in medium entropy equiatomic alloys (MEAs) with less than 5 components such as CoNiCr, $Fe_{40}Mn_{40}Co_{10}Cr_{10}$, $Fe_{50}Mn_{30}Co_{10}Cr_{10}$, and a number of others, high physical and mechanical properties are observed. During deformation, especially at low temperatures, several deformation mechanisms operate in these alloys, such as twinning and phase transformations, known as the TWIP and TRIP mechanisms [32–34]. The effect of TWIP and TRIP mechanisms in coarse-grained HEAs $Fe_{40}Mn_{40}Co_{10}Cr_{10}$, $Fe_{50}Mn_{30}Co_{10}Cr_{10}$ in a wide temperature range (300–0.5 K) was first studied in our early work [35–37]. It was shown that in these HEAs in the coarse-grained state under uniaxial tension in the temperature range of 0.5–4.2 K, due to the action of the TWIP and TRIP mechanisms, strength of ≈ 1.5–1.8 GPa and plasticity of ≈ 65–85% were achieved and this far exceeds similar values in traditional alloys. It is obvious that the use of the TRIP and TWIP mechanisms in HEA opens up many potential possibilities for creating cryogenic high-strength materials. However, despite intensive studies of these alloys, many aspects of the deformation of these materials remain insufficiently studied. In particular, it is of great interest to study the processes of grain structure refinement of TWIP and TRIP alloys under severe plastic deformation (SPD) and the possibility of increasing their strength by creating a nanostructured state. In this respect, the present work is devoted to a study of the structure and mechanical properties of TWIP $Fe_{40}Mn_{40}Co_{10}Cr_{10}$ alloy and TRIP $Fe_{50}Mn_{30}Co_{10}Cr_{10}$ alloy after SPD at 300 K and 77 K by high-pressure torsion (HPT). The HPT method has been widely used in many works to obtain a nanostructured state in a number of HEAs [16, 38–43] and can be effectively used to study microstructure evolution and phase transformations caused by deformations [44, 45]. In addition, one of the tasks of the work is to study the stability of the microstructure formed after HPT deformation at 300 and 77 K, depending on long-term storage under ambient conditions (atmospheric pressure, in air at room temperature).

2. Materials and methods of research

Nonequiatomic high-entropy alloys $Fe_{40}Mn_{40}Co_{10}Cr_{10}$ (TWIP) and $Fe_{50}Mn_{30}Co_{10}Cr_{10}$ (TRIP) were obtained by arc melting of elements at low pressure in a high-purity argon atmosphere inside a cooled water copper plate. The purity of the alloying elements was above 99.9 at. %. In order to ensure chemical homogeneity, the ingots were remelted at least 5 times. After casting, homogenization annealing was carried out in an argon atmosphere at 1000 °C for 24 h. The blanks were then rolled at room temperature into a tape 1 mm thick with a reduction of 10–15% per pass with intermediate annealing at a temperature of 1000 °C for 1 h after 50–60% reduction. Disks with 10 mm in diameter were cut from the tape, and then mechanically ground to a thickness of 0.9 mm and annealed at a temperature of 1000 °C for 1 h. The HPT method was used to obtain the nanostructural state. The applied HPT deformation technique at 300 (RT-HTP) and 77 K (cryo-HTP) was similar to that described in detail in [41]. The temperature of 77 K was obtained by immersion of the sample and the HPT-plungers in liquid nitrogen. Straight radial lines were attached to the upper and lower surfaces of the samples, which could also be identified after the HPT processing, and the rotation angle fully coincided with the monitored rotations of the plunger. This indicated that no slip occurred during HPT processing; moreover, such a slip event would have led to a sudden decrease in the torque curves, but such decreases were never observed (Fig. 6). The in situ torques during the HPT process were measured by two V-shaped strain gauges connected as full bridges. These strain gauges were diagonally arranged on a hollow cylinder made of steel supporting the nonrotating, fixed HPT anvil, being part of the HPT facility used. After appropriate calibration, the nominal electronic torque resolution was 0.01 nm, whereas the electronic measuring noise was about a factor of 10 higher. For the shear stress derived, this means a measuring resolution of distinctly below 1 MPa. Values of shear strain were calculated by using the equation [41]

$$\gamma = 2\pi nr / h, \quad (1)$$

where n is the number of rotations, r is the distance from the rotation axis, and h is the sample thickness achieved after HPT processing ($h = 0.8$ mm). The plungers were rotated at a rate of 0.2 rpm, which corresponds to the maximum shear strain rate during torsion $d\gamma/dt = 0.11$ s^{-1}. The number of rotations n was 0.25 and 5. For the measurement of microhardness H_v, the HPT discs were mechanically polished. Using a PAAR MHD and PMT microhardness tester equipped with a Vickers indenter, a load of 1.5 N was applied for 15 s, and indentations were achieved in distances of 0.5 mm along four different radial directions of the disc from the center to the edge. The microhardness H_v values obtained at the same distance from the center were

averaged over four values and plotted on the corresponding graphs. Microhardness measurements were carried out two hours after HPT and one year under ambient conditions (atmospheric pressure, in air at room temperature). Specimens for mechanical testing with a size of 0.6×0.6×1.2 mm were cut out from the edge part of the disks (in the uniform deformation area), which were subjected to five revolutions ($n = 5$). Samples were deformed by uniaxial compression with a relative loading rate of 10^{-4} s^{-1} at room temperature (300 K) and liquid nitrogen temperature (77 K).

Overall structural characteristics of the alloys were studied using synchrotron radiation. Diffraction patterns were collected at a distance of 4.5 mm from the center of the disk in the region of a homogeneous structure. The size of the diffraction area was 0.5×0.5 mm. Diffraction patterns are presented as $I = f(Q)$, where I is intensity, $Q = 4\pi \sin\theta/\lambda$ is the scattering vector, λ is the radiation wavelength, θ is the diffraction angle. The phase composition and structural characteristics of the samples were determined by the Rietveld method (Maud software). The study of microstructural parameters: $<\varepsilon>$ is average microstrain, D is the size of the coherent scattering domains (CSD), or crystallite size is based on the line profile analysis (LPA). These parameters have different contributions to the broadening of diffraction peaks:

$$\beta_L = \frac{\lambda}{D\cos\theta}, \quad \beta_G = 4 < \varepsilon > \tan\theta, \qquad (2)$$

where β_L, β_G are the Lorentzian and Gaussian components of the Voightian profile, respectively. The instrumental broadening correction was done by a polycrystalline CeO_2 powder sample. From the FWHM (full width at half maximum) values an instrumental resolution function was obtained, with the help of which the true physical broadening β was determined from the total peaks broadening of the studied samples.

3. Results and discussion

3.1. Structural characteristics of nanostructured alloys

In the initial state, the $Fe_{40}Mn_{40}Co_{10}Cr_{10}$ TWIP alloy contained one fcc phase, while the TRIP $Fe_{50}Mn_{30}Co_{10}Cr_{10}$ alloy was two-phase and contained 59 vol.% fcc phase and 41 vol % hcp phase [36, 37]. The diffraction patterns of both alloys subjected to RT-HTP and cryo-HPT temperatures are shown in Fig. 1.

As seen in Fig. 1, after HPT deformation in the TWIP $Fe_{40}Mn_{40}Co_{10}Cr_{10}$ and TRIP $Fe_{50}Mn_{30}Co_{10}Cr_{10}$ alloys, two phases are observed: fcc and hcp, and only in one case (after RT-HTP at $n = 5$) the $Fe_{50}Mn_{30}Co_{10}Cr_{10}$ alloy contains 100% hcp phases [Fig. 1(g)]. An analysis of the intensity distribution of diffraction peaks indicates the presence of texture in all samples. Grains of the hcp phase are preferably oriented along the {10.0} crystallographic planes parallel to the sample surface, and for the fcc phase along the {100} planes. An analysis of the broadening and profile shape of the hcp phase peaks showed that (10.2), (10.3), (10.4) peaks are more broadened and have long tails, which may indicate the presence of twins in the structure. Therefore, for the hcp phase, we estimated the twin faults probability (tfp) using the Warren model [46]. Note that peak broadening after HPT deformation may be associated with lattice deformation due to the formation of new lattice defects and a decrease in grain size [47]. All results on the phase composition and microstructural characteristics of the studied TWIP $Fe_{40}Mn_{40}Co_{10}Cr_{10}$ and TRIP $Fe_{50}Mn_{30}Co_{10}Cr_{10}$ alloys are given in Table 1.

From the data presented in Table 1, it follows that in the studied alloys, as a result of HPT deformation, complex structural changes occur, depending on the HPT temperature and the number of revolutions n. Note the main features of the structure evolution in the $Fe_{50}Mn_{30}Co_{10}Cr_{10}$ and $Fe_{40}Mn_{40}Co_{10}Cr_{10}$ alloys.

Feature 1. HPT deformation leads to an increase in the microhardness H_v, i.e., to a significant hardening of the investigated alloys. For the TWIP $Fe_{40}Mn_{40}Co_{10}Cr_{10}$ alloy, the microhardness ratio for the coarse-grained and nanostructured states (for RT-HTP , $n = 5$) is approximately 3.7, and for the TRIP $Fe_{50}Mn_{30}Co_{10}Cr_{10}$ alloy, this ratio is 2.1, i.e., the effect of hardening in the TWIP $Fe_{40}Mn_{40}Co_{10}Cr_{10}$ alloy is even more pronounced. It can be seen from Fig. 2 that for samples in the nanostructured state, there is a decrease in the HPT temperature and an increase in n for all the cases studied, leading to an increase in the value of H_v.

Feature 2. HPT deformation leads to significant changes in the phase composition. The composition of the hcp and fcc phases in the TRIP $Fe_{50}Mn_{30}Co_{10}Cr_{10}$ and TWIP $Fe_{40}Mn_{40}Co_{10}Cr_{10}$ alloys after RT-HTP and cryo-HPT at $n = 0.25$ and $n = 5$ is graphically shown in Fig. 3.

For TWIP $Fe_{40}Mn_{40}Co_{10}Cr_{10}$ it was found that the single-phase fcc alloy in the initial state becomes a two-phase one after HPT deformation. As can be seen from Fig. 2, the content of the hcp phase after RT-HTP at $n = 0.25$, i.e., at low shear strain ($\gamma = 8.84$) reaches 83.4% and noticeably more (almost 96%) after cryo-HPT. With a further increase in the number of revolutions to $n = 5$ ($\gamma = 177$), however, an insignificant decrease in the hcp phase (by 1.6–2%) is observed at both HPT temperatures. Note that the content of the fcc phase after cryo-HPT is three times less than after RT-HTP for both $n = 0.25$ and 5 (Fig. 3). The TRIP $Fe_{50}Mn_{30}Co_{10}Cr_{10}$ alloy in the initial state contains two phases. For $n = 0.25$ the content of the hcp phase increases after RT-HTP to 89.7% and after cryo-HPT to 96.5%. With an increase in the number of revolutions to $n = 5$, the samples become practically single-phase — the content of the hcp phase is 100% for RT-HTP and 98.5% for cryo-HPT, respectively.

Feature 3. The microstructure parameters (D, $<\varepsilon>$, tfp for hcp and fcc phases) depend on the HPT temperature and the number of revolutions n. Moreover, as can be seen from Fig. 4, the crystallite size D in fcc and hcp phase are different.

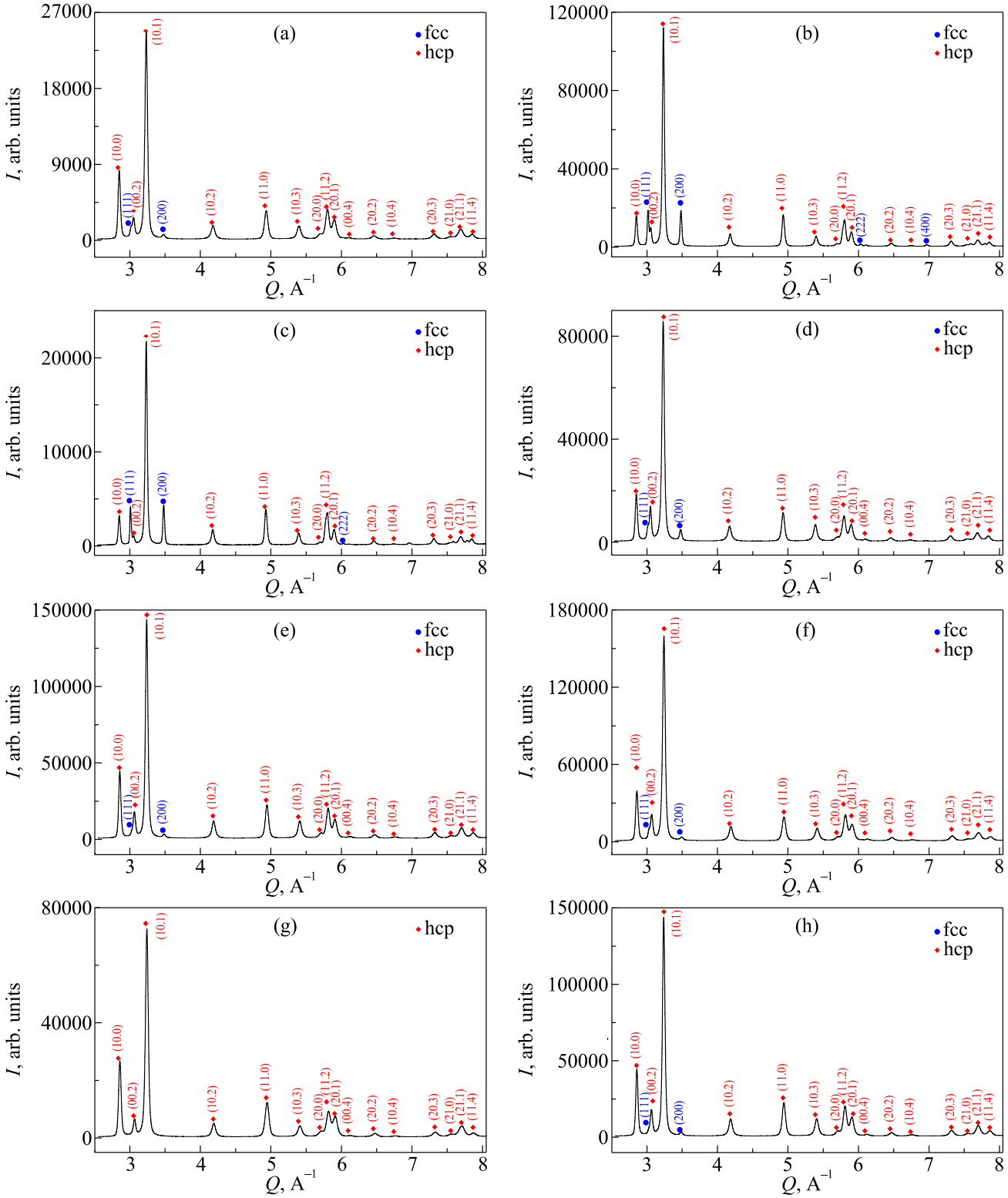

Fig. 1. (Color online) Diffraction patterns. For the $Fe_{40}Mn_{40}Co_{10}Cr_{10}$ alloy: RT-HTP, $n = 0.25$ (a), cryo-HPT, $n = 0.25$ (b), RT-HTP, $n = 5$ (c), cryo-HPT, $n = 5$ (d). For the $Fe_{50}Mn_{30}Co_{10}Cr_{10}$ alloy: RT-HTP, $n = 0.25$ (e), cryo-HPT, $n = 0.25$ (f), RT-HTP, $n = 5$ (g), cryo-HPT, $n = 5$ (h).

Table 1. Phase composition and structural characteristics of the studied TRIP $Fe_{50}Mn_{30}Co_{10}Cr_{10}$ and TWIP $Fe_{40}Mn_{40}Co_{10}Cr_{10}$ alloys, after RT-HTP and cryo-HPT for the number of revolutions $n = 0.25$ and 5. The H_v and γ values are given at $r = 4.5$ mm from the center of the samples. Dashes correspond to the cases, where the microstructural characteristics could not be determined. The structural characteristics for alloys in the initial state ($n = 0$) are taken from [36, 37]

Sample	n	γ	Temperature HPT, K	Phase	Fraction, vol %	Lattice parameters, Å	Microstructural parameters			H_v, GPa
							D, nm	$10^3 < \varepsilon >$	10^3 tfp	
TWIP initial	0	0		hcp	0					
				fcc	100	3.624				1.31
TRIP initial	0	0		hcp	41.0	$a = 2.542$, $c = 4.104$				2.48
				fcc	59.0	3.604	215.0	< 0.5		
TWIP-HPT	0.25	8.84	300	hcp	83.4	$a = 2.546$, $c = 4.114$	48.7	2.24	4.1	4.15
				fcc	16.6	3.608	87.2	1.95	–	
			77	hcp	95.9	$a = 2.546$, $c = 4.113$	42.4	3.4	6.9	4.26
				fcc	4.1	3.611	–	–	–	
	5	177	300	hcp	81.8	$a = 2.546$, $c = 4.113$	54.0	2.24	4.3	4.78
				fcc	18.2	3.609	74.7	1.66	–	
			77	hcp	93.9	$a = 2.547$, $c = 4.122$	42.4	2.96	6.8	5.41
				fcc	6.1	3.613	34.1	1.64	–	
TRIP-HPT	0.25	8.84	300	hcp	89.7	$a = 2.544$, $c = 4.103$	53.5	2.99	5.2	4.37
				fcc	10.3	3.601	42.6	1.78	–	
			77	hcp	96.5	$a = 2.543$, $c = 4.099$	44.2	3.64	6.4	4.85
				fcc	3.5	3.598	–	–	–	
	5	177	300	hcp	100	$a = 2.543$, $c = 4.106$	42.7	4.03	4.1	5.15
				fcc	0	–	–	–	–	
			77	hcp	98.5	$a = 2.543$, $c = 4.106$	59.6	3.45	5.4	5.59
				fcc	1.5	3.605	–	–	–	

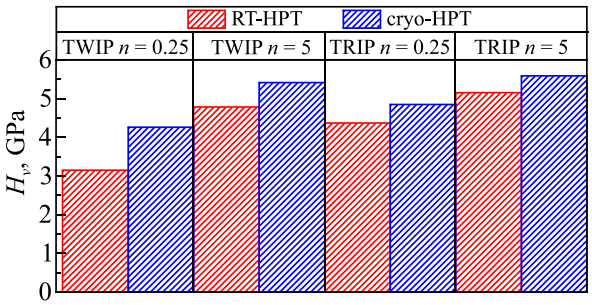

Fig. 2. (Color online) The value of microhardness H_v in the TRIP $Fe_{50}Mn_{30}Co_{10}Cr_{10}$ and the TWIP $Fe_{40}Mn_{40}Co_{10}Cr_{10}$ alloys after RT-HTP and cryo-HPT at $n = 0.25$ and 5.

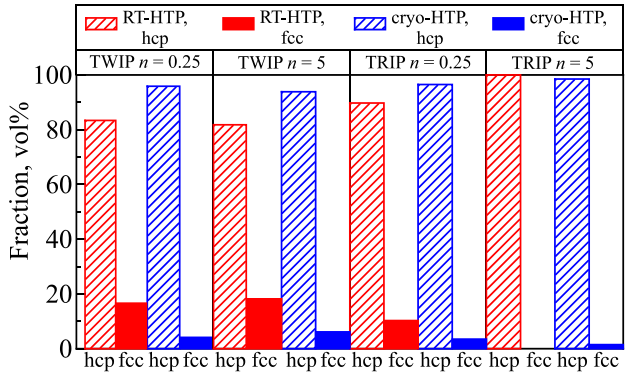

Fig. 3. (Color online) Composition of hcp and fcc phases in the TRIP $Fe_{50}Mn_{30}Co_{10}Cr_{10}$ and the TWIP $Fe_{40}Mn_{40}Co_{10}Cr_{10}$ alloys after RT-HTP and cryo-HPT at $n = 0.25$ and 5.

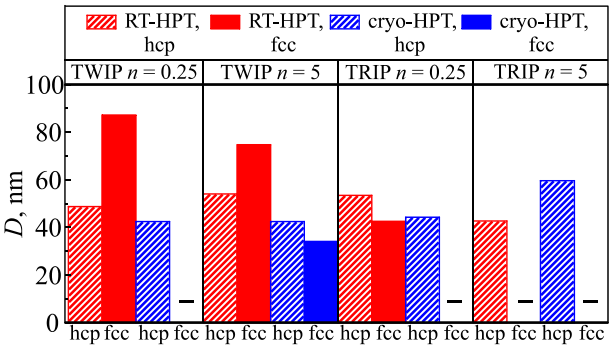

Fig. 4. (Color online) The value of crystallite sizes D in the TRIP $Fe_{50}Mn_{30}Co_{10}Cr_{10}$ and the TWIP $Fe_{40}Mn_{40}Co_{10}Cr_{10}$ alloys after RT-HTP and cryo-HPT at $n = 0.25$ and 5. Dashes correspond to cases when it was not possible to determine the D values due to the low content of the fcc phase.

The greatest difference is observed in the structure of the TWIP $Fe_{40}Mn_{40}Co_{10}Cr_{10}$ alloy after RT-HTP: the value of D in the fcc phase is 87.2 nm and thus 1.8 times greater than in the hcp phase (48.7 nm). It is found for both alloys that for the hcp phase with decreasing HPT temperature the values of D tend to decrease. This trend, however, does not hold for the TRIP $Fe_{50}Mn_{30}Co_{10}Cr_{10}$ alloy subjected to 5 turns of torsion (D is 42.7 and 59.6 nm for deformation at 300 and 77 K temperatures, respectively). In the TWIP $Fe_{40}Mn_{40}Co_{10}Cr_{10}$ alloy, a decrease in the parameter D for the fcc phase is also observed with a decrease in the

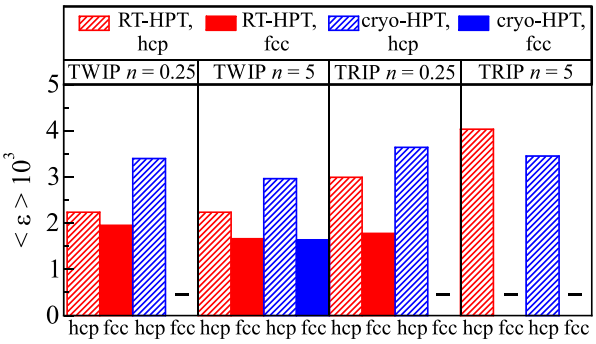

Fig. 5. (Color online) Microstrain $<\varepsilon>$ for hcp and fcc phases in the TRIP $Fe_{50}Mn_{30}Co_{10}Cr_{10}$ and the TWIP $Fe_{40}Mn_{40}Co_{10}Cr_{10}$ alloys after RT-HTP and cryo-HPT at $n = 0.25$ and 5. Dashes correspond to the cases when due to the low content of the fcc phase, the $<\varepsilon>$ values could not be determined.

deformation temperature, and this parameter has the smallest value 34.1 nm for the case of $n = 5$, cryo-HPT. For the hcp phase, an explicit dependence of D on the number of revolutions has not been established. Apparently, for the hcp phase already at $\gamma \geq 8.84$, this parameter changes slightly and is close to saturation ($D = 42$–54 nm).

As can be seen in Fig. 5, the value $<\varepsilon>$ in the hcp phase in the TRIP $Fe_{50}Mn_{30}Co_{10}Cr_{10}$ alloy is higher than that in the TWIP $Fe_{40}Mn_{40}Co_{10}Cr_{10}$ alloy. For the case $n = 0.25$ in both alloys, $<\varepsilon>$ increases with a decrease in the HPT temperature. At $n = 5$ such growth is observed only in the TWIP $Fe_{40}Mn_{40}Co_{10}Cr_{10}$. Note also that tfp increases with decreasing HPT temperature. In addition, for $n = 5$ for both HPT temperatures, the tfp values for the $Fe_{40}Mn_{40}Co_{10}Cr_{10}$ TWIP are higher than those for the $Fe_{50}Mn_{30}Co_{10}Cr_{10}$ TRIP alloy, as shown in Table 1.

Feature 4. Lattice parameters.

It should be noted that the lattice parameters of both phases for TWIP $Fe_{40}Mn_{40}Co_{10}Cr_{10}$ samples are slightly larger than the corresponding values for TRIP $Fe_{50}Mn_{30}Co_{10}Cr_{10}$ samples, which may be due to the high content of Mn where the metallic radius of which $r = 1.27$ Å is larger than that of Fe ($r = 1.26$ Å).

3.2. Mechanical characteristics of nanostructured $Fe_{40}Mn_{40}Co_{10}Cr_{10}$ and $Fe_{50}Mn_{30}Co_{10}Cr_{10}$ alloys

3.2.1. Torsional shear stress

Figure 6 shows plots of shear stress τ versus strain γ obtained from torque data measured in situ during the RT-HTP and cryo-HPT processes. Such in situ measurements, as noted in Sec. 2, indicate the magnitude of the deforming stress during shear deformation, and make it possible to control the absence of slippage occurring between the sample and plungers during the torsion of the sample. It can be seen that during the deformation of TWIP $Fe_{40}Mn_{40}Co_{10}Cr_{10}$ and TRIP $Fe_{50}Mn_{30}Co_{10}Cr_{10}$ TWIP alloys, the value of τ for all γ in the cryo-HPT process is greater than the value of τ in

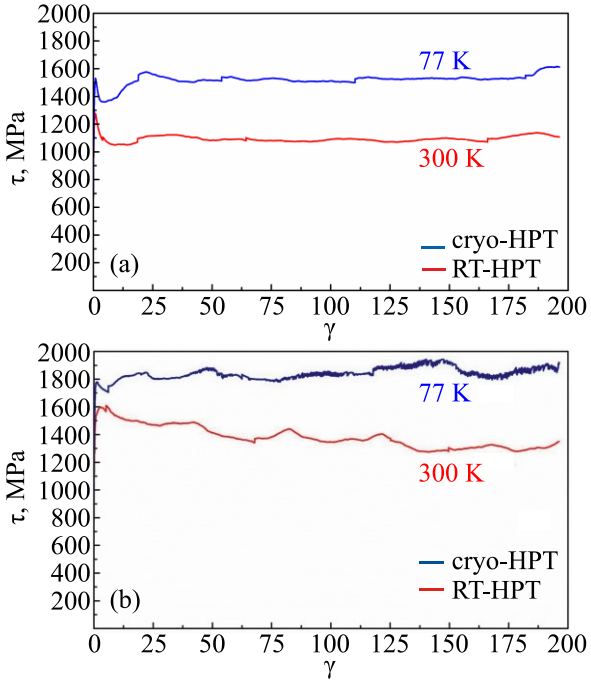

Fig. 6. (Color online) Torsional shear stress as derived from the torque data measured in situ during 300 K and 77 K HPT-processing for nanostructured: the $Fe_{40}Mn_{40}Co_{10}Cr_{10}$ alloy (a), the $Fe_{50}Mn_{30}Co_{10}Cr_{10}$ alloy (b).

the RT-HTP process. At $\gamma > 20$ in the TWIP alloy, the dependencies $\tau(\gamma)$ reach a plateau. In the TRIP $Fe_{50}Mn_{30}Co_{10}Cr_{10}$ alloy, with increasing γ, the value of τ at cryo-HPT, on average, slightly increases, and, on average, decreases at RT-HTP. The value of τ is larger for the TRIP $Fe_{50}Mn_{30}Co_{10}Cr_{10}$ deformation than for TWIP $Fe_{40}Mn_{40}Co_{10}Cr_{10}$, both for cryo-HPT and RT-HTP.

3.2.2. Dependencies of microhardness on different parameters for nanostructured the $Fe_{40}Mn_{40}Co_{10}Cr_{10}$ and the $Fe_{50}Mn_{30}Co_{10}Cr_{10}$ alloys

Figure 7 shows the H_v values for TRIP $Fe_{50}Mn_{30}Co_{10}Cr_{10}$ and TWIP $Fe_{40}Mn_{40}Co_{10}Cr_{10}$ alloys in the initial state, measured along the sample diameter. The practical absence of the dependence H_v (l) indicates the homogeneity of the structure in the initial coarse-grained samples of these alloys. It can be seen that the TRIP $Fe_{50}Mn_{30}Co_{10}Cr_{10}$ alloy is stronger than the TWIP $Fe_{40}Mn_{40}Co_{10}Cr_{10}$ alloy. The ratio of the microhardness values of these alloys (H_v -TRIP/ H_v -TWIP) is 1.89. For comparison, Fig. 7 also shows the dependence H_v (l) for the Cantor alloy studied in detail in the literature [5, 12–16].

For the convenience of comparing the microstructural parameters of TRIP $Fe_{50}Mn_{30}Co_{10}Cr_{10}$ and TWIP $Fe_{40}Mn_{40}Co_{10}Cr_{10}$ alloys, Figs. 8 and 9 show the dependencies $H_v(r)$ and $H_v(\gamma)$, respectively, for the range $r > 2$. Here, the value of H_v is practically independent of r (or γ), which corresponds to a region with a homogeneous microstructure in the sample. Note that, according to relation (1), due to the gradient distribution of the shear strain from the

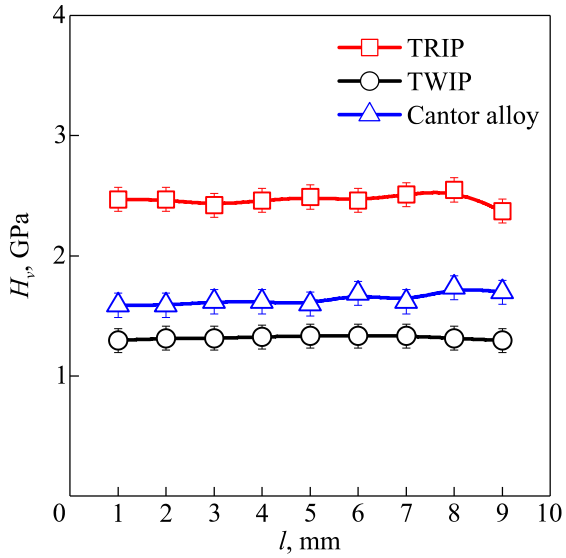

Fig. 7. (Color online) Microhardness H_v depending on the distance l along the disk diameter for the samples in the initial state, for different alloys: TRIP $Fe_{50}Mn_{30}Co_{10}Cr_{10}$ (□), TWIP $Fe_{40}Mn_{40}Co_{10}Cr_{10}$ (○), Cantor CoCrFeMnNi (△) [48].

center of the samples to its edges, a gradient microstructure is formed in the samples which arises due to the inhomogeneous dynamic crushing of grains [49, 50]. Therefore, in the region of small radii $r < 2$, an increase in the value of H_v is observed, and for the region $r > 2$, the value of H_v reaches a plateau. This form of the dependence $H_v(r)$ and $H_v(\gamma)$ has been experimentally confirmed for many materials [38–43, 48]. Figure 8 for TRIP $Fe_{50}Mn_{30}Co_{10}Cr_{10}$ and TWIP $Fe_{40}Mn_{40}Co_{10}Cr_{10}$ alloys for a region of homogeneous microstructure presents the dependencies of the value of $H_v(r)$ for $n = 0.25$ and 5. It can be seen that, in TRIP $Fe_{50}Mn_{30}Co_{10}Cr_{10}$ [Figs. 8(a) and 8(b)] and TWIP $Fe_{40}Mn_{40}Co_{10}Cr_{10}$ [Figs. 8(c) and 8(d)] alloys, an increase in n leads to an increase in the value of H_v.

Figure 9 shows the dependencies $H_v(\gamma)$ for $n = 5$. It can be seen that in the $Fe_{50}Mn_{30}Co_{10}Cr_{10}$ TRIP alloy, in the region of a homogeneous microstructure, a decrease in the HPT temperature from 300 to 77 K leads to an increase in the microhardness by an average of 10%. In contrast to this, for the $Fe_{40}Mn_{40}Co_{10}Cr_{10}$ TWIP alloy, a similar decrease in the HPT temperature leads to a slight (within the spread of experimental data) increase in the microhardness value for the region $\gamma > 150$.

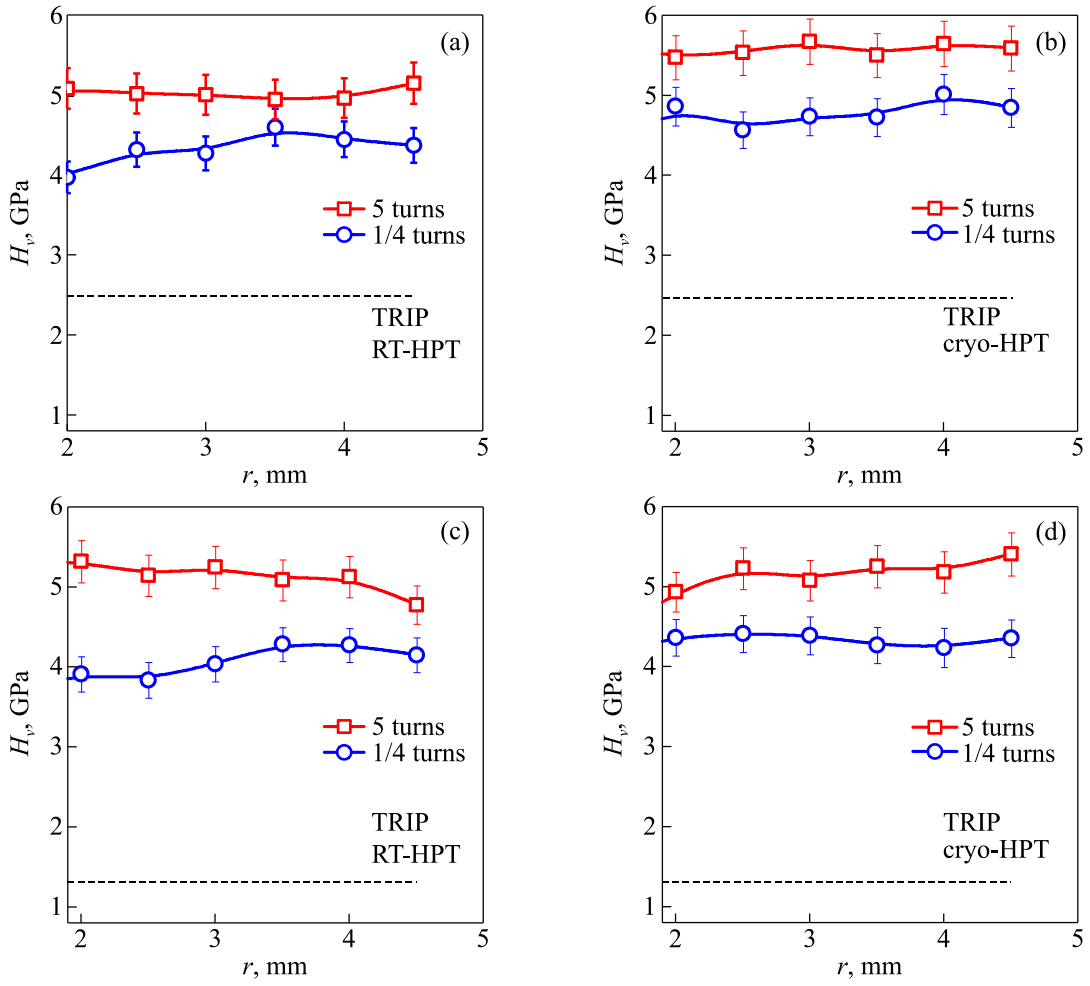

Fig. 8. (Color online) Microhardness H_v depending on the distance from the disk center r. For the $Fe_{50}Mn_{30}Co_{10}Cr_{10}$ alloy: RT-HTP (a), cryo-HPT (b); for the $Fe_{40}Mn_{40}Co_{10}Cr_{10}$ alloy: RT-HTP (c), cryo-HPT (d); $n = 5$ (□), $n = 0.25$ (○). Dotted line initial state.

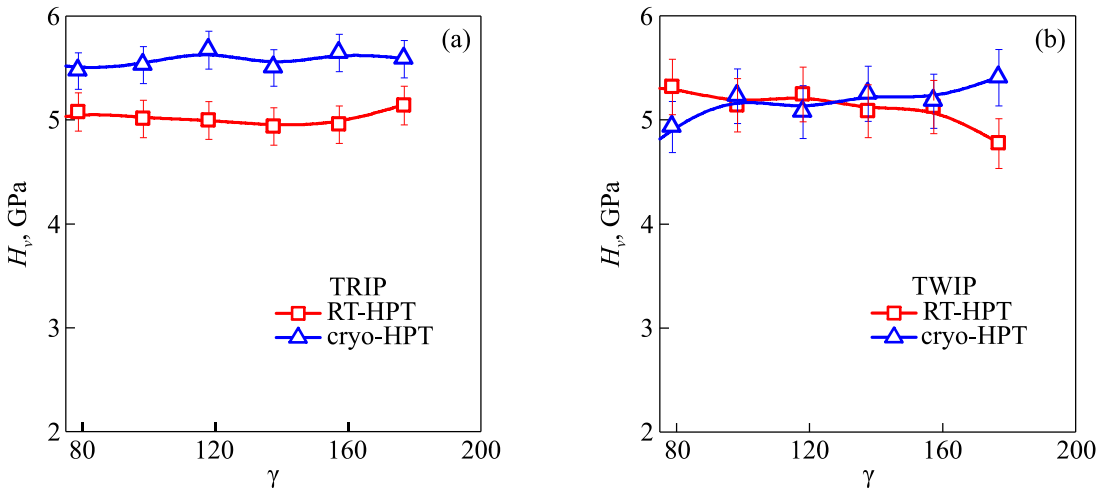

Fig. 9. (Color online) Microhardness H_v depending on the shear strain γ for the $Fe_{50}Mn_{30}Co_{10}Cr_{10}$ and $Fe_{40}Mn_{40}Co_{10}Cr_{10}$ alloys for different HPT temperatures: $Fe_{50}Mn_{30}Co_{10}Cr_{10}$ (a), $Fe_{40}Mn_{40}Co_{10}Cr_{10}$ (b); cryo-HPT (△), RT-HTP (□), $n = 5$.

Figure 10 for nanograined $Fe_{40}Mn_{40}Co_{10}Cr_{10}$ and $Fe_{50}Mn_{30}Co_{10}Cr_{10}$ alloys (for samples after RT-HTP and cryo-HPT, $n = 5$) shows the dependencies of $H_v(\gamma)$ on different sample holding times (within 2 hours and for one year) under ambient conditions (atmospheric pressure, in air at room temperature). It can be seen that for the cases shown in Fig. 10(a), (c), the $H_v(\gamma)$ dependencies almost coincide. For the alloy $Fe_{50}Mn_{30}Co_{10}Cr_{10}$ (cryo-HPT), aging for one year led to a slight decrease in the level of the microhardness [Fig. 10(d)]. Such a decrease in the microhardness values can be associated with the reverse transitions from the hcp to the fcc phase during the aging of the samples after the HPT deformation. Note that such reverse transformations from the hcp to the fcc phase after HPT deformation were observed in a number of cases in the Cantor alloy [56].

Thus, the above results show that $Fe_{50}Mn_{30}Co_{10}Cr_{10}$ and $Fe_{40}Mn_{40}Co_{10}Cr_{10}$ nanocrystalline alloys aged at room temperature for one year remain stable in most cases considered.

3.2.3. Mechanical characteristics under active loading of nanostructured $Fe_{40}Mn_{40}Co_{10}Cr_{10}$ *and* $Fe_{50}Mn_{30}Co_{10}Cr_{10}$ *alloys*

Samples for deformation by uniaxial compression were cut from the edge part of the disks (in the uniform deformation area) being subjected to HPT deformation at 300 and 77 K. Figure 11 shows the deformation curves for the TWIP alloy $Fe_{40}Mn_{40}Co_{10}Cr_{10}$, obtained by uniaxial compression with a relative loading rate of 10^{-4} s^{-1} at room temperature (300 K) and liquid nitrogen temperature (77 K) for nanostructured samples after RT-HTP [Fig. 11(a)] and after cryo-HPT [Fig. 11(b)].

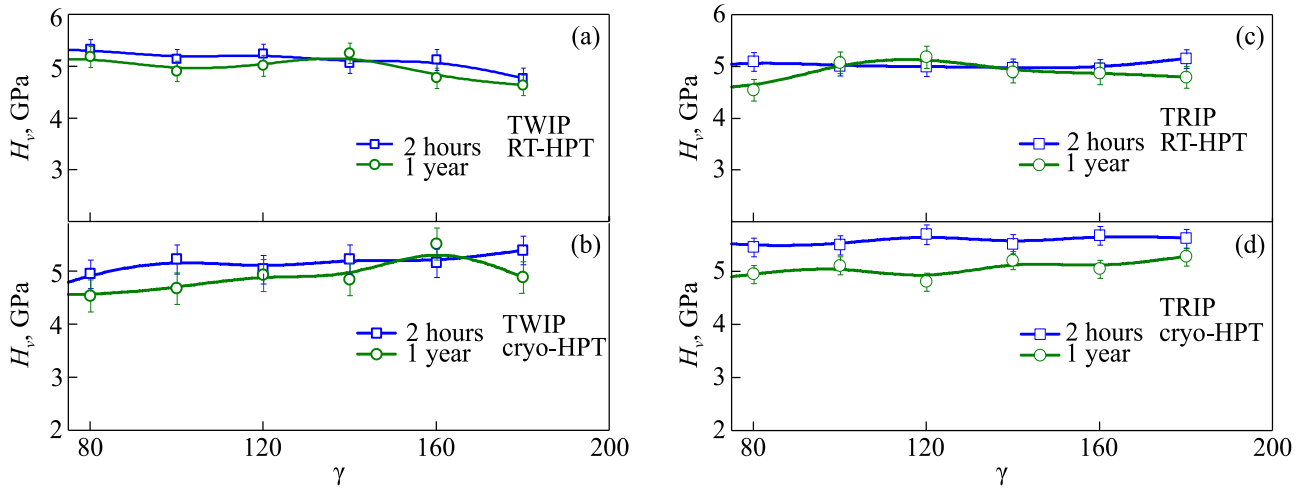

Fig. 10. (Color online) Microhardness H_v depending on the shear strain γ for different adding time f ambient storage. For the $Fe_{40}Mn_{40}Co_{10}Cr_{10}$ alloy: RT-HTP (a), cryo-HPT (b); for the $Fe_{50}Mn_{30}Co_{10}Cr_{10}$ alloy: RT-HTP (c), cryo-HPT (d); 2 hours (□), 1 year (○).

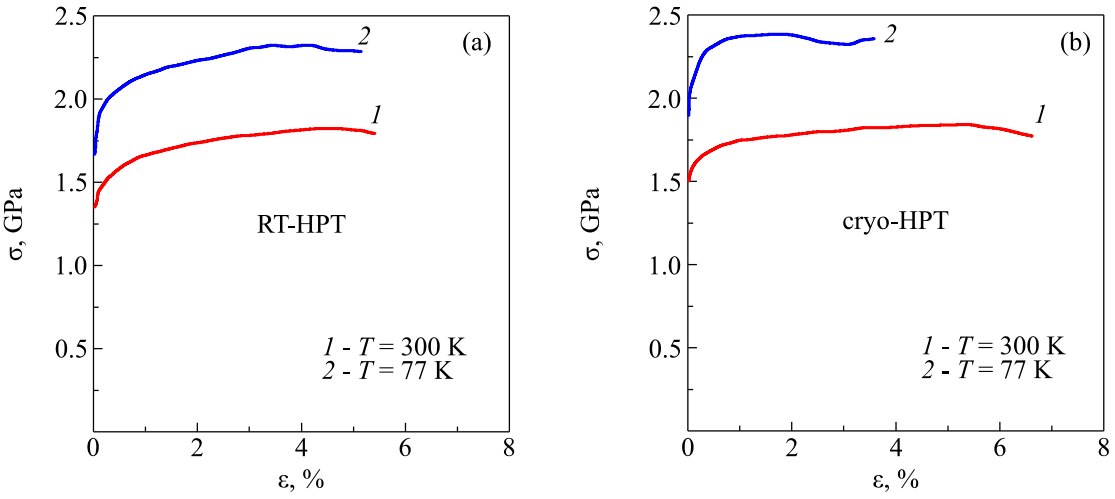

Fig. 11. (Color online) The deformation curves for nanostructured samples of the $Fe_{40}Mn_{40}Co_{10}Cr_{10}$ alloy after RT-HTP (a) and after cryo-HPT (b), strain rate 10^{-4} s^{-1}; compression at 300 K (*1*), compression at 77 K (*2*).

The parameters of the deformation curves (yield strength $\sigma_{0.2}$, ultimate strain ε_{max}, ultimate strength σ_U) for the $Fe_{40}Mn_{40}Co_{10}Cr_{10}$ alloy shown in Fig. 11 are given in Table 2. For comparison, Table 2 also shows the corresponding parameters for samples in the coarse-grained material [36]. As can be seen from the data given in Table 2, the transition from a coarse-grained to a nanostructured state leads to a significant increase in the yield strength and tensile strength with a decrease in the plasticity resource. Unlike the nanostructured TWIP $Fe_{40}Mn_{40}Co_{10}Cr_{10}$, the nanostructured TRIP $Fe_{50}Mn_{30}Co_{10}Cr_{10}$ alloys completely lose plasticity under uniaxial compression at 300 K. The samples were destroyed in the elastic region at stresses of ≈ 630 MPa. The main cracks with numerous smaller lateral cracks appear along the loading axis in the specimens. Obviously, the observed loss of plasticity in the nanostructured state is associated with an increase in the fraction of grain boundaries and the impossibility of relaying shear deformation from grain to grain.

Table 2. Mechanical characteristics of the $Fe_{40}Mn_{40}Co_{10}Cr_{10}$ alloy in the nanostructured state tested under uniaxial compression, and in an initial state [36] tested under uniaxial tension at a rate of 10^{-4} s^{-1}, for deformation temperatures of 300 K and 77 K. The HPT temperature is 300 K (RT-HTP) and 77 K (cryo-HPT)

Sample	Compression temperature, K	$\sigma_{0.2}$, GPa	ε_{max}, %	σ_U, GPa
Initial	300	0.19	46	0.75
	77	0.41	46	1.71
RT-HTP	300	1.49	5.38	1.82
	77	1.97	5.15	2.32
cryo-HPT	300	1.62	6.62	1.84
	77	2.17	3.5	2.38

4. Significance of the results

We like to discuss the experimental data obtained for nanostructured alloys TWIP $Fe_{40}Mn_{40}Co_{10}Cr_{10}$ and TRIP $Fe_{50}Mn_{30}Co_{10}Cr_{10}$ in the form of the following points:

Point 1. Comparison of data on the structure of the samples (synchrotron X-ray studies yielding phase composition, lattice parameters, etc.) obtained after three years after HPT deformation with structures obtained immediately after HPT shows that the microstructure of the studied TWIP $Fe_{40}Mn_{40}Co_{10}Cr_{10}$ and TRIP $Fe_{50}Mn_{30}Co_{10}Cr_{10}$ alloys did basically not change during the storage at ambient temperature and atmospheric pressure. This stability of the microstructure is also reflected by the dependencies $H_v(\gamma)$ measured two hours and one year after HPT deformation (Fig. 10).

Point 2. A decrease in the HPT temperature from 300 K to 77 K leads to an increase in both the torsional shear stress τ (Fig. 6) and the H_v values (in the region of a homogeneous microstructure) (Fig. 8). In addition, in the $Fe_{40}Mn_{40}Co_{10}Cr_{10}$ alloy, with a decrease in the deformation temperature during uniaxial compression, the yield strength also increases (Fig. 11). This temperature dependence of these strength values indicates the thermally activated nature of plastic deformation in the $Fe_{40}Mn_{40}Co_{10}Cr_{10}$ TWIP alloy. Previously, the thermally activated nature of plastic deformation was established for the coarse-grained state in the $Fe_{40}Mn_{40}Co_{10}Cr_{10}$ and in the $Fe_{50}Mn_{30}Co_{10}Cr_{10}$ alloys [36, 37].

Point 3. Comparison of data on microstructural parameters and mechanical properties of TWIP $Fe_{40}Mn_{40}Co_{10}Cr_{10}$ and TRIP $Fe_{50}Mn_{30}Co_{10}Cr_{10}$ alloys in the initial coarse-grained and nanostructured states indicates their significant changes as a result of HPT deformation. If for the coarse-grained state, the values of microhardness H_v and yield stress $\sigma_{0.2}$ differ significantly between TWIP $Fe_{40}Mn_{40}Co_{10}Cr_{10}$ and

TRIP $Fe_{50}Mn_{30}Co_{10}Cr_{10}$ alloys, (H_v -TRIP/ H_v -TWIP = 1.89 in Fig. 7, $\sigma_{0.2}$-TRIP/$\sigma_{0.2}$-TWIP = 1.3 [36, 37]), then after HPT deformation achieving nanostructures, these differences, both in microhardness and in phase composition, practically disappear, as shown in Figs. 3 and 10. In both alloys, hardening is observed as a result of the increasing appearance of the harder hcp phase, of strong grain crushing according to the Hall-Petch relation, and of the appearance of twins in significant density. In the structure of both alloys, the hcp phase predominates, the content of which does not depend very strongly on the temperature T and the number of revolutions n during the HPT. Note that, for the TRIP $Fe_{50}Mn_{30}Co_{10}Cr_{10}$ alloy in the coarse-grained state after active tensile deformation at T = 300 and 77 K, in regions close to the fracture surface, a complete phase transition of the fcc lattice to hcp is observed [37]. A similar result for a TRIP $Fe_{50}Mn_{30}Co_{10}Cr_{10}$ alloy of the same composition was also reported [28]. It is shown that active tensile deformation at 300 K, due to the fcc-hcp phase transition, leads to an appearance the of a 98% hcp phase [28]. In contrast to the TRIP alloy, in the coarse-grained TWIP $Fe_{40}Mn_{40}Co_{10}Cr_{10}$ alloy as a result of active tensile deformation (under similar conditions), the volume fraction of the formed hcp phase does not exceed 50% [36]. The corresponding data obtained earlier [36, 37] for coarse-grained TWIP $Fe_{40}Mn_{40}Co_{10}Cr_{10}$ and TRIP $Fe_{50}Mn_{30}Co_{10}Cr_{10}$ alloys are given in Table 3.

Point 4. As is known [51–54], the probability of TWIP or TRIP processes occurring during plastic deformation in metallic materials depends significantly on the stacking fault energy (SFE). At SFE from 20 mJ/m^2 to 40 mJ/m^2, TWIP processes are activated, and at SFE values below 20 mJ/m^2, TRIP processes are activated. Such a dependence is due to the influence of the SFE value on the dissociation of dislocations in the course of deformation. It has been shown [55, 56] that the nucleation of a new phase occurs by rupture of dissociated 1/2<110> dislocations, thus, the easier it is, so the lower the SFE. In this case, the phase transformation during the HPT occurs almost at the speed of sound, since the partial dislocations involved in the phase transformation have a kinetic energy much higher than under quasi-static conditions [55]. It is assumed [57] that in two-phase (fcc + hcp) HEAs, the hcp phase increases strength, while the fcc phase increases plasticity. New boundaries arising during the phase transition prevent the motion of dislocations [58–60] and lead to strain hardening of these alloys. In the course of HPT large shear deformations lead to the simultaneous action of several deformation mechanisms [61, 62], as a result of which the initial differences in the structure of alloys and their strength, observed in coarse-grained TWIP $Fe_{40}Mn_{40}Co_{10}Cr_{10}$ and TRIP $Fe_{50}Mn_{30}Co_{10}Cr_{10}$ alloys, are significantly reduced, which was observed in this work.

One of the significant differences in the properties of the nanostructured alloys studied in this work is the absence of macroscopic ductility in the TRIP $Fe_{50}Mn_{30}Co_{10}Cr_{10}$ alloy under active compression deformation, while the TWIP $Fe_{40}Mn_{40}Co_{10}Cr_{10}$ alloy remains ductile under a similar deformation (Fig. 11). Apparently, the reason for the embrittlement of the TRIP $Fe_{50}Mn_{30}Co_{10}Cr_{10}$ alloy is the high concentration in comparison with the TWIP $Fe_{40}Mn_{40}Co_{10}Cr_{10}$ alloy, of highly distorted local regions with a high level of local stresses and lattice microdeformations (Fig. 5). It is obvious that microcracks can appear in such regions, which prevent the occurrence of macroscopic plastic deformation in samples deformed by compression and this leads to the destruction of samples before reaching the macroscopic yield strength. Thus, a comparison of the structure and mechanical properties of the nanostructured TWIP $Fe_{40}Mn_{40}Co_{10}Cr_{10}$ and TRIP $Fe_{50}Mn_{30}Co_{10}Cr_{10}$ alloys showed that both alloys have high strength, but macroscopic plasticity is retained only in the TWIP $Fe_{40}Mn_{40}Co_{10}Cr_{10}$ alloy. For a more detailed search for the reasons leading to the embrittlement of the TRIP $Fe_{50}Mn_{30}Co_{10}Cr_{10}$ alloy during its macroscopic deformation, it is necessary to conduct additional microstructural studies. The results obtained confirm the importance of taking into account the TRIP or TWIP effects and the SFE value when designing high-strength materials based on MEA or HEA alloys.

Table 3. Phase composition of coarse-grained TRIP $Fe_{50}Mn_{30}Co_{10}Cr_{10}$ and TWIP $Fe_{40}Mn_{40}Co_{10}Cr_{10}$ alloys in the initial state and after active deformation by uniaxial tension [36, 37]

Alloy	State	Phase	Volume fraction, %	Lattice parameter, Å
TRIP $Fe_{40}Mn_{40}Co_{10}Cr_{10}$	initial	fcc	59.0	3.607
		hcp	41.0	a = 2.552, c = 4.107
	deformed at 295 K	fcc	6.0	3.614
		hcp	94.0	a = 2.550, c = 4.112
	deformed at 77 K	fcc	2.7	3.614
		hcp	97.3	a = 2.549, c = 4.111
TWIP $Fe_{50}Mn_{30}Co_{10}Cr_{10}$	initial	fcc	100	3.618
	deformed at 295 K	fcc	72	3.628
		hcp	28	a = 2.558, c = 4.123
	deformed at 77 K	fcc	33	3.625
		hcp	67	a = 2.552, c = 4.119

5. Summary and Conclusions

The results of this work can be summarized as follows:

(1) As results of HPT deformation, in the TWIP $Fe_{40}Mn_{40}Co_{10}Cr_{10}$ and TRIP $Fe_{50}Mn_{30}Co_{10}Cr_{10}$ alloys, a basically complete phase transition from the fcc phase to hcp phase is observed, the content of which does not depend very strongly on the HPT temperature and the number of revolutions n in HPT.

(2) HPT deformation leads to a significant reduction in differences in phase composition and in the microhardness values for TWIP and TRIP alloys observed in the coarse-grained state.

(3) HPT deformation leads to a significant increase in the microhardness H_v, and in the TWIP $Fe_{40}Mn_{40}Co_{10}Cr_{10}$ alloy this effect is more pronounced than in the TRIP $Fe_{50}Mn_{30}Co_{10}Cr_{10}$ alloy. A decrease in the HPT temperature and an increase in HPT revolution number (i.e. deformation) for all the cases studied lead to an increase in the value of H_v.

(4) It was found that the microstructure of nanostructured samples of TWIP $Fe_{40}Mn_{40}Co_{10}Cr_{10}$ and TRIP $Fe_{50}Mn_{30}Co_{10}Cr_{10}$ alloys remains stable for a long time.

(5) It has been established that the $Fe_{40}Mn_{40}Co_{10}Cr_{10}$ TWIP alloy remains ductile under active compression deformation at 300 and 77 K, while there is no macroscopic plasticity in the $Fe_{50}Mn_{30}Co_{10}Cr_{10}$ TRIP alloy under similar conditions.

(6) It has been established that in the $Fe_{40}Mn_{40}Co_{10}Cr_{10}$ TWIP alloy the thermally activated character of plastic deformation is retained during the transition from the coarse-grained to the nanostructured state.

M.A.T. and A.V.L. were supported by the National Research Foundation of Ukraine in frame of the project No. 2020.02/0327.

1. J. W. Yeh, S. K. Chen, S. J. Lin, J. Y. Gan, T. S. Chin, T. T. Shun, C. H. Tsau, and S. Y. Chang, *Adv. Eng. Mater.* **6**, 299 (2004).
2. B. Cantor, I. T. H. Chang, P. Knight, and A. J. B. Vincent, *Mater. Sci. Eng. A* **375**, 213 (2004).
3. Y. Deng, C. C. Tasan, K. G. Pradeep, H. Springer, A. Kostka, and D. Raabe, *Acta Mater.* **94**, 124 (2015).
4. O. N. Senkov, G. B. Wilks, J. M. Scott, and D. B. Miracle, *Intermetallics* **19**, 698 (2011).
5. E. P. George, D. Raabe, and R. O. Ritchie, *Nature Rev. Mater.* **4**, 515 (2019).
6. S. L. Wei, S. J. Kim, J. Y. Kang, Y. Zhang, Y. J. Zhang, T. Furuhara, E. S. Park, and C. C. Tasan, *Nature Mater.* **19**, 1175 (2020).
7. N. T. Nguyen, P. Asghari-Rad, P. Sathiyamoorthi, A. Zargaran, C. S. Lee, and H. S. Kim, *Nature Comm.* **11**, 2736 (2020).
8. K. F. Gan, D. S. Yan, S. Y. Zhu, and Z. M. Li, *Acta Mater.* **206**, 116633 (2021).
9. W. D. Li, D. Xie, D. Y. Li, Y. Zhang, Y. F. Gao, and P. K. Liaw, *Prog. Mater. Sci.* **118**, 100777 (2021).
10. H. Shahmir, M. S. Mehranpour, S. A. A. Shams and T. G. Langdon, *J. Mater. Res. Tech.* **23**, 3362 (2023).
11. A. D. Pogrebnjak, A. A. Bagdasaryan, I. V. Yakushchenko, and V. M. Beresnev, *Russ. Chem. Rev.* **83**, 1027 (2014).
12. B. Gludovatz, A. Hohenwarter, D. Catoor, E. H. Chang, E. P. George, and R. O. Ritchie, *Science* **345**, 1153 (2014).
13. G. Laplanche, J. Bonneville, C. Varvenne, W. A. Curtin, and E. P. George, *Acta Mater.* **143**, 257 (2018).
14. Q. Q. Ding, X. Q. Fu, D. K. Chen, H. B. Bei, B. Gludovatz, J. X. Li, Z. Zhang, E. P. George, Q. Yu, T. Zhu, and R. O. Ritchie, *Mater. Today* **25**, 21 (2019).
15. A. V. Podolskiy, E. Schafler, E. D. Tabachnikova, M. A. Tikhonovsky, and M. J. Zehetbauer, *Fiz. Nizk. Temp.* **44**, 1245 (2018) [*Low Temp. Phys.* **44**, 976 (2018)].
16. B. B. Bian, N. Guo, H. J. Yang, R. P. Guo, L. Yang, Y. C. Wu, and J. W. Qia, *Alloys Compd.* **827**, 153981 (2020).
17. A. Hirata, S. X. Song, T. G. Nieh, P. K. Liaw, C. T. Liu, and M. W. Chen, *Acta Mater.* **144**, 107 (2018).
18. R. Feng, M. C. Gao, C. Zhang, W. Guo, J. D. Poplawsky, F. Zhang, J. A. Hawk, J. C. Neuefeind, Y. Ren, and P. K. Liaw, *Acta Mater.* **146**, 280 (2018).
19. S. S. Nene, M. Frank, K. Liu, R. S. Mishra, B. A. McWilliams, and K. C. Cho, *Sci. Rep.* **8**, 9920 (2018).
20. N. D. Stepanov, D. G. Shaysultanov, R. S. Chernichenko, D. M. Ikornikov, V. N. Sanin, and S. V. Zherebtsov, *Mater. Sci. Eng. A* **728**, 54 (2018).
21. Q. H. Fang, Y. Chen, J. Li, C. Jiang, B. Liu, Y. Liu, and P. K. Liaw, *Int. J. Plast.* **114**, 161 (2019).
22. C. C. Tasan, M. Diehl, D. Yan, M. Bechtold, F. Roters, L. Schemmann, C. Zheng, N. Peranio, D. Ponge, M. Koyama, K. Tsuzaki, and D. Raabe, *Ann. Rev. Mater. Res.* **45**, 391 (2015).
23. S. Singh, N. Wanderka, B. S. Murty, U. Glatzel, and J. Banhart, *Acta Mater.* **59**, 182 (2011).
24. Z. Lei, X. Liu, Y. Wu, H. Wang, S. Jiang, S. Wang, X. Hui, Y. Wu, B. Gault, P. Kontis, D. Raabe, L. Gu, Q. Zhang, H. Chen, H. Wang, J. Liu, K. An, Q. Zeng, T. G. Nieh, and Z. Lu, *Nature* **563**, 546 (2018).
25. Z. Wu, H. Bei, G. M. Pharr, and E. P. George, *Acta Mater.* **81**, 428 (2014).
26. G. Laplanche, A. Kostka, C. Reinhart, J. Hunfeld, G. Eggeler, and E. P. George, *Acta Mater.* **128**, 292 (2017).
27. Z. Li and D. Raabe, *JOM* **69**, 11 (2017).
28. Z. Li, C. C. Tasan, K. G. Pradeep, and D. Raabe, *Acta Mater.* **131**, 323 (2017).
29. T. Gao, X. Jin, J. Qiao, H. Yang, Y. Zhang, and Y. Wu, *J. Appl. Phys.* **129**, 175101 (2021).
30. C. Wei, Y. Lu, X. Du, T. Li, T. Wang, and P. K. Liaw, *Mater. Sci. Eng. A* **818**, 141446 (2021).
31. T. Yang, Y. L. Zhao, J. H. Luan, B. Han, J. Wei, J. J. Kai, and C. T. Liu, *Scripta Mater.* **164**, 30 (2019).
32. S. Yang, Y. Yang, and H. Wang, *Adv. Eng. Mater.* **22**, 1900868 (2019).
33. E. D. Tabachnikova, A. V. Podolskiy, M. O. Laktionova, N. A. Bereznaia, M. A. Tikhonovsky, and A. S. Tortika, *J. Alloys Compd.* **698**, 501 (2017).

34. S. J. Sun, Y. Z. Tian, H. R. Lin, X. G. Dong, Y. H. Wang, Z. J. Zhang, and Z. F. Zhang, *Mater. Des.* **133**, 122 (2017).
35. J. Moon, E. Tabachnikova, S. Shumilin, T. Hryhorova, Y. Estrin, J. Brechtl, P. K. Liaw, K. A. Dahmen, A. Zargaran, J. W. Bae, H. S. Do, B.-J. Lee, and H. S. Kim, *Phys. Rev. Mater.* **5**, 083601 (2021).
36. T. V. Hryhorova, S. E. Shumilin, Yu. O. Shapovalov, Yu. O. Semerenko, O. D. Tabachnikova, M. A. Tikhonovsky, A. S. Tortika, M. J. Zehetbauer, and E. Schafler, *J. V. N. Karazin Kharkiv National University, Ser. Phys.* **32**, 41 (2020).
37. E. D. Tabachnikova, T. V. Hryhorova, S. E. Shumilin, I. V. Kolodiy, Yu. O. Shapovalov, Yu. O. Semerenko, S. N. Smirnov, I. V. Kashuba, M. A. Tikhonovsky, M. I. Zehetbauer, and E. Schafler, *Fiz. Nizk. Temp.* **48**, 955 (2022) [*Low Temp. Phys.* **48**, 845 (2022)].
38. H. Shahmir, E. Tabachnikova, A. Podolskiy, M. Tikhonovsky, and T. G. Langdon, *J. Mater. Sci.* **53**, 11813 (2018).
39. A. V. Levenets, H. V. Rusakova, L. S. Fomenko, Y. Huang, I. V. Kolodiy, R. L. Vasilenko, E. D. Tabachnikova, M. A. Tikhonovsky, T. G. Langdon, *Fiz. Nizk. Temp.* **48**, 629 (2022) [*Low Temp. Phys.* **48**, 560 (2022)].
40. X. Liu, H. Ding, Y. Huang, X. Bai, Q. Zhang, H. Zhang, T. G. Langdon, and J. Cui, *J. Alloys Compd.* **867**, 159063 (2021).
41. A. V. Podolskiy, Y. O. Shapovalov, E. D. Tabachnikova, A. S. Tortika, M. A. Tikhonovsky, B. Joni, E. Ódor, T. Ungar, S. Maier, C. Rentenberger, M. J. Zehetbauer, and E. Schafler, *Adv. Eng. Mater.* **22**, 1900752 (2020).
42. Yu. O. Shapovalov, E. D. Tabachnikova, M. A. Tikhonovsky, A. V. Levenets, M. J. Zehetbauer, and E. Schafler, *J. V. N. Karazin Kharkiv National University, Ser. Phys.* **32**, 59 (2020).
43. J. Moon, E. Tabachnikova, S. Shumilin, T. Hryhorova, Yu. Estrin, J. Brechtl, P. K. Liaw, W. Wang, K. A. Dahmen, A. Zargaran, J. W. Bae, H.-S. Do, B.-J. Lee, and H. Seop Kim, *Materials Today* **50**, 55 (2021).
44. R. Z. Valiev, Y. Estrin, Z. Horita, T. G. Langdon, M. J. Zehetbauer, and Y. Zhu, *JOM* **68**, 1216 (2016).
45. K. Edalati and Z. Horita, *Mater. Sci. Eng. A* **652**, 325 (2016).
46. B. E. Warren, *Progress in Metal Physics* **8**, 147 (1959).
47. K. Nakagawa, M. Hayashi, K. Takano-Satoh, H. Matsunaga, H. Mori, K. Maki, Y. Onuki, S. Suzuki, and S. Sato, *Quantum Beam Sci.* **4**, 36 (2020).
48. H. V. Rusakova, L. S. Fomenko, S. N. Smirnov, A. V. Podolskiy, Y. O. Shapovalov, E. D. Tabachnikova, M. A. Tikhonovsky, A. V. Levenets, M. J. Zehetbauer, and E. Schafler, *Mater. Sci. Eng. A* **828**, 142116 (2021).
49. A. Heczel, M. Kawasaki, J. L. Lábár, J.-il Jang, T. G. Langdon, and J. Gubicza, *J. Alloy. Compd.* **711**, 143 (2017).
50. B. Schuh, F. Mendez-Martin, B. Völker, E. P. George, H. Clemens, R. Pippan, and A. Hohenwarter, *Acta Mater.* **96**, 258 (2015).
51. S. L. Wong, M. Madivala, U. Prahl, F. Roters, and D. Raabe, *Acta Mater.* **118**, 151 (2016).
52. J. Su, X. Wu, D. Raabe, and Z. Li, *Acta Mater.* **167**, 23 (2019).
53. S. Allain, J.-P. Chateau, O. Bouaziz, S. Migot, and N. Guelton, *Mater. Sci. Eng. A* **387**, 158 (2004).
54. T.-H. Lee, E. Shin, C.-S. Oh, H.-Y. Ha, and S.-J. Kim, *Acta Mater.* **58**, 3173 (2010).
55. P. Haasen, *Physical Metallurgy, 3rd ed.*, Cambridge University Press, Cambridge, UK (1995), p. 327.
56. R. Chulist, A. Pukenas, P. Chekhonin, A. Hohenwarter, R. Pippan, N. Schell, and W. Skrotzki, *Materials* **15**, 8407 (2022).
57. P. Edalati, A. Mohammadi, M. Ketabchi, and K. Edalati, *J. Alloys Compd.* **894**, 162413 (2022).
58. Q. Fang, Y. Chen, J. Li, C. Jiang, B. Liu, Y. Liu, and P. K. Liaw, *Int. J. Plast.* **114**, 161 (2019).
59. X. Li, D. L. Irving, and L. Vitos, *Sci. Rep.* **8**, 11196 (2018).
60. E. Welsch, D. Ponge, S. M. Hafez Haghighat, S. Sandlöbes, P. Choi, M. Herbig, S. Zaefferer, and D. Raabe, *Acta Mater.* **116**, 188 (2016).
61. I. Gutierrez-Urrutia and D. Raabe, *Acta Mater.* **60**, 5791 (2012).
62. X. Wu, D. Mayweg, D. Ponge, and Z. Li, *Mater. Sci. Eng. A* **802**, 140661 (2021).

Структура та кріогенно-механічні властивості сильно деформованих нееквіатомних сплавів системи Fe–Mn–Co–Cr

E. D. Tabachnikova, T. V. Hryhorova, S. N. Smirnov, I. V. Kolodiy, Yu. O. Shapovalov, A. V. Levenets, S. E. Shumilin, I. V. Kashuba, M. A. Tikhonovsky, F. Spieckermann, M. J. Zehetbauer, E. Schafler, Y. Huang, T. G. Langdon

Досліджено структури та механічні властивості двох нееквіатомних середньоентропійних нанокристалічних сплавів, в яких у крупнозернистому стані під час пластичної деформації діють додаткові механізми — двійникування (TWIP) у $Fe_{40}Mn_{40}Co_{10}Cr_{10}$ та фазові перетворення (TRIP) в $Fe_{50}Mn_{30}Co_{10}Cr_{10}$. Нанокристалічний стан у цих сплавах досягається крутінням під високим тиском (НРТ) при 300 та 77 К при кількості обертів $n = 0.25$ та $n = 5$. У нанокристалічному стані у досліджених сплавах спостерігається, в основному, повний фазовий перехід від ГЦК до ГЩП ґратки, вміст якого не залежить від температури та деформації НРТ. У вивчених сплавах у нанокристалічному стані спостерігається суттєве зменшення відмінностей у фазовому складі та мікротвердості H_v, які спостерігаються у цих сплавах у крупнозернистому стані. Зниження температури та збільшення деформації НРТ для всіх досліджених випадків призводять до збільшення значення H_v. TWIP сплав $Fe_{40}Mn_{40}Co_{10}Cr_{10}$ залишається пластичним при активній деформації стиску при 300 та 77 К, тоді як у TRIP $Fe_{50}Mn_{30}Co_{10}Cr_{10}$ сплаві за аналогічних умов макроскопічна пластичність відсутня. При переході від крупнозернистого до нанокристалічного стану у TWIP $Fe_{40}Mn_{40}Co_{10}Cr_{10}$ сплаві зберігається термоактиваційний характер пластичної деформації.

Ключові слова: високоентропійні сплави, мікроструктура, кріогенні температури, механічні властивості.